Journal of Marine Science and Engineering

MDPI

Article

Self-Tuning Inductance-Oriented Model-Free Predictive Current Control for Tidal Stream Turbines

Mengjia Cui [1], Tianzhen Wang [1,*], Xueli Wang [1], Demba Diallo [2] and Xuefang Lin-Shi [3]

1 Logistics Engineering College, Shanghai Maritime University, Pudong District, Shanghai 201306, China; 202330210118@stu.shmtu.edu.cn (M.C.); xl.wang@shmtu.edu.cn (X.W.)
2 Group of Electrical Engineering Paris, CentraleSupelec, Centre National de la Recherche Scientifique (CNRS), Université Paris Saclay, 91192 Gif Sur Yvette, France; demba.diallo@centralesupelec.fr
3 Ampere (UMR 5005), INSA Lyon, Ecole Centrale de Lyon, Université Claude Bernard Lyon 1, Centre National de la Recherche Scientifique (CNRS), 69621 Villeurbanne, France; xuefang.shi@insa-lyon.fr
* Correspondence: tzwang@shmtu.edu.cn; Tel.: +86-1351-219-9500

Abstract

Tidal energy is increasingly harnessed due to its high energy density, substantial reserves, and reliable predictability. However, marine fouling on turbine blades adds weight and induces asymmetric system loads; prolonged operation exacerbates generator magnetic saturation, causing inductance parameter deviations from controller presets, which further leads to current loop delays, amplified tracking errors and unstable power output. To mitigate these issues, a self-tuning inductance-oriented model-free predictive current control method is proposed. The proposed method utilizes a simplified hyperlocal model alongside an extended state observer to effectively counteract the effects of non-inductive parameters. Simultaneously, the incremental model coupled with a dynamic adjustment method is proposed for real-time adaptive inductance tuning. Simulation results demonstrate that the proposed method significantly enhances system robustness against inductance mismatches and reduces parameter sensitivity, thereby ensuring stable operation. Compared with traditional PI control and model predictive control strategies, the proposed approach exhibits superior performance in disturbance rejection, parameter adaptability, and operational stability.

Keywords: tidal energy; inductance mismatch; self-tuning inductance; permanent magnet synchronous generator; model predictive control

1. Introduction

Global energy production relies heavily on fossil fuels, exacerbating issues such as climate change, air pollution, and challenges to energy security [1]. Meanwhile, the share of renewable energy in the power system is steadily increasing [2]. Marine energy generation technologies, including tidal energy, wave energy, and ocean thermal energy, are being actively explored [3], with tidal energy receiving particular attention due to its high energy density, abundant reserves, and predictability [4]. Operating in harsh underwater environments [5], the tidal stream turbine (TST) faces extreme conditions such as swells, turbulence, strong storms, and biofouling. Long-term fluctuations in tidal stream velocity exacerbate system fatigue and may further trigger magnetic circuit saturation and demagnetization effects, leading to nonlinear changes in inductance [6,7]. Current prediction errors and torque control deviations in the control algorithms of the permanent

Academic Editor: Eugen Rusu

Received: 16 February 2026
Revised: 12 March 2026
Accepted: 19 March 2026
Published: 22 March 2026

magnet synchronous generator (PMSG) are directly caused by parameter mismatch, posing a significant threat to the operational accuracy and stability of the system [8,9].

To achieve stable operation under fluctuating tidal velocities, various advanced control strategies have been applied to the tidal stream turbine (TST), including adaptive control [10], fuzzy control [11], and H_∞ robust control [12]. However, their practical adoption is often hindered by the harsh marine environment, high maintenance costs, and demanding reliability standards. These constraints critically limit the applicability of computationally complex or parameter-sensitive algorithms. Within the typical control hierarchy, maximum power point tracking (MPPT) methods, such as power feedback control [13] and hill-climbing search [14], generate the optimal torque or speed reference. Meanwhile, torque regulation strategies like direct torque control (DTC) [15] and field-oriented control (FOC) [16] are tasked with accurate reference tracking. Nevertheless, these torque controllers, along with direct power control (DPC) [17], often suffer from power ripples or parameter sensitivity, which induce mechanical stress on the drivetrain and threaten the system's longevity. At the higher-level speed/power control loop, strategies such as fixed-time integral terminal sliding mode control combined with an adaptive RBF neural network [18] offer fast convergence and robustness. Despite these advantages, their direct implementation faces potential limitations due to the heavy computational burden of online learning. At the critical current control level, the common PI controller lacks robustness, prompting the development of advanced alternatives: active disturbance rejection control (ADRC) [19] and its linear variant (LADRC) [20] enhance disturbance rejection but require complex tuning. An improved linear-nonlinear switching ADRC (LNSADRC) [21] and a robust adaptive super-twisting controller [22] offer enhanced robustness but may struggle with chattering or parameter sensitivity. Fuzzy logic control (FLC) [23] and fractional-order fuzzy controllers [24] provide good tracking but can exhibit insufficient robustness or high computational load. Model predictive current control (MPCC) [25] enhances dynamic performance but incurs high computational cost and model dependency. Unmodelled predictive current control (UM-MPCC) [26] reduces this dependency, though its long-term stability requires further validation. While extended state observer (ESO)-based predictive control [27] combines real-time estimation with precision, its performance can be compromised by inductance mismatch. Conversely, parameter-robust predictive current control [28] effectively handles variations, while adaptive methods like online parameter identification [29] and iterative sliding mode observers [30] tackle mismatch at the cost of increased computational overhead. In summary, existing solutions face a critical trade-off: conventional controllers often fail under parameter mismatch, while adaptive methods typically incur excessive computational costs. This highlights a pressing need for control strategies that balance high performance, robustness, and ease of implementation to ensure reliable TST operation.

To address the issues of inductance mismatch, current loop delay, and unstable power output caused by magnetic saturation from prolonged asymmetric loading in the tidal stream turbine (TST), a novel self-tuning inductance-oriented model-free predictive current control (STI-MFPCC) is proposed to ensure stable system operation under both matched and mismatched inductance conditions. The innovative features of the method include: (1) adopting an incremental model to reduce parameter dependency and establishing an inductance tuning mechanism based on the linear relationship between prediction error and current increment, thereby solving the challenges associated with real-time identification and compensation for dynamic inductance variations; and (2) simplifying the system structure using an ultra-local model, and combining an extended state observer with model-free current control principles to compute the rotor reference voltage vector, thus overcoming the reliance on precise mathematical models and complex parameter tuning in conventional methods. The proposed approach overcomes the drawbacks of traditional model predictive control, such as parameter sensitivity and complex tuning, offering a robust, low-complexity, and easily implementable solution for the permanent magnet synchronous generator (PMSG) system, ultimately ensuring stable operation of the TST under inductance mismatch conditions.

This article proceeds as follows: Section 2 describes the system model and problem formulation; Section 3 outlines the proposed self-tuning inductance-oriented model-free predictive current control; Section 4 presents the RT-LAB real-time simulation results; and Section 5 concludes the paper.

2. General and Problem Description of TST

A tidal power generation system is a highly complex and nonlinear dynamic system. Its complexity stems not only from the strong dynamic coupling among the hydrodynamic, mechanical, and electrical domains, but also from the stochastic fluctuations of tidal currents and the asymmetric loads experienced by the turbine during long-term operation. The system primarily comprises a turbine, a permanent magnet synchronous generator (PMSG), a machine-side AC-DC converter, a DC bus, and a grid-side DC-AC converter. Within this configuration, the aforementioned operational stressors jointly induce complex phenomena such as magnetic circuit saturation within the generator. Consequently, key system parameters (e.g., inductance) exhibit time-varying and mismatched characteristics during actual operation, which in turn introduces severe control challenges, such as the degradation of current loop dynamics and power oscillations. A tidal power generation system is a highly complex and nonlinear dynamic system. Its complexity stems not only from the strong dynamic coupling among the hydrodynamic, mechanical, and electrical domains, but also from the stochastic fluctuations of tidal currents and the asymmetric loads experienced by the turbine during long-term operation. The system primarily comprises a turbine, a permanent magnet synchronous generator (PMSG), a machine-side AC-DC converter, a DC bus, and a grid-side DC-AC converter. Within this configuration, the aforementioned operational stressors jointly induce complex phenomena such as magnetic circuit saturation within the generator. Consequently, key system parameters (e.g., inductance) exhibit time-varying and mismatched characteristics during actual operation, which in turn introduces severe control challenges, such as the degradation of current loop dynamics and power oscillations.

2.1. Mathematical Modeling of the TST

As the core energy conversion component within the tidal power generation system, the TST is specifically designed to capture kinetic energy from tidal currents and convert it into mechanical energy. According to Betz's theory, the mechanical power P_m and the mechanical torque T_m extracted by the turbine can be expressed as follows [31]:

$$\begin{cases} P_m = \frac{1}{2}\rho\pi R^2 v^3 C_p(\lambda,\beta) \\ T_m = \frac{P_m}{\omega} \end{cases} \tag{1}$$

Furthermore, the power coefficient $C_p(\lambda,\beta)$ can be empirically approximated as follows [32,33].

$$\begin{cases} C_p(\lambda,\beta) = 0.5176\left(\frac{116}{\lambda_i} - 0.4\beta - 5\right)e^{-\frac{24}{\lambda_i}} + 0.0068\lambda \\ \frac{1}{\lambda_i} = \frac{1}{\lambda+0.08\beta} - \frac{0.035}{\beta^3+1} \end{cases} \tag{2}$$

where β denotes the pitch angle.

This concise mathematical framework lays the theoretical foundation for analyzing the operational challenges inherent to the tidal power generation system.

2.2. Problem Description for TST

Although the ideal mathematical model of the PMSG provides a baseline for system analysis, its actual operation is subject to multiple disturbances, such as blade biofouling and magnetic saturation. These factors in turn induce inductance mismatch and further compromise the operational stability of the entire system. In the synchronously rotating d-q reference frame, the voltage equations for the PMSG are expressed as [34]:

$$\begin{cases} u_d = R_s i_d + L_d \frac{\mathrm{d}i_d}{\mathrm{d}t} - n_p \omega_n L_q i_q \\ u_q = R_s i_q + L_q \frac{\mathrm{d}i_q}{\mathrm{d}t} + n_p \omega_n (L_d i_d + \psi_f) \end{cases} \tag{3}$$

Correspondingly, the motion equations of the PMSG can be expressed as follows:

$$\begin{cases} T_e = \frac{3}{2} n_p i_q \left[(L_d - L_q) i_d + \psi_f \right] \\ J \frac{\mathrm{d}\omega_n}{\mathrm{d}t} = T_m - T_e - B\omega_n \end{cases} \tag{4}$$

In this study, it is assumed that a surface-mounted PMSG (SPMSG) is utilized; therefore, $L_d = L_q = L_s$. where u_d and u_q denote the d-axis and q-axis components of the stator voltage, i_d and i_q the d-axis and q-axis components of the stator current, R_s the stator resistance, L_d and L_q the d-axis and q-axis stator inductances, ψ_f the permanent magnet flux linkage, n_p the number of pole pairs, ω_n the rotor mechanical angular velocity, T_e the electromagnetic torque, J the combined moment of inertia, T_m the mechanical torque from the prime mover, and B the viscous friction coefficient. It is assumed that the PMSG is a surface-mounted type. Therefore, $L_d = L_q = L_s$.

To maximize energy capture, the hydrodynamic design of TST blades is often heavily optimized using detailed 3D-CFD analyses, such as adjusting the stroke angle of blades and incorporating winglets [35]. Despite these ideal mechanical enhancements, during actual long-term operation, tidal power generator units are inevitably prone to biofouling or debris entanglement on their blades. Biofouling significantly increases blade mass and surface roughness [36], degrading their hydrodynamic performance and causing system asymmetric loads [37]. Long-term operation under such asymmetric loads can exacerbate magnetic circuit saturation in the generator, manifested as nonlinear saturation characteristics of the d-axis and q-axis inductances with increasing current [8], as shown below:

$$\begin{cases} L_d(i_d, i_q) = L_{d0} \cdot e^{-k_d (i_d^2 + i_q^2)} \\ L_q(i_d, i_q) = L_{q0} \cdot e^{-k_q (i_d^2 + i_q^2)} \end{cases} \tag{5}$$

where $k_d > 0, k_q > 0$, and L_{d0} and L_{q0} represent the rated inductances.

Consequently, the actual inductances deviate from the nominal design values [38], leading to dynamic response delays, phase shifts, and increased steady-state errors Δi_q in the stator current. As illustrated in Figure 1, under scenarios where the inductance L_s reaches 1.2 times its nominal value, this current deviation directly induces an electromagnetic torque error ΔT_e. In cases where $|\Delta T_e| < |\Delta T_m|$, the angular velocity fluctuations $\Delta\omega$ are amplified. A sustained increase in $\Delta\omega$ eventually compromises the stability of the power output, ultimately threatening overall system integrity.

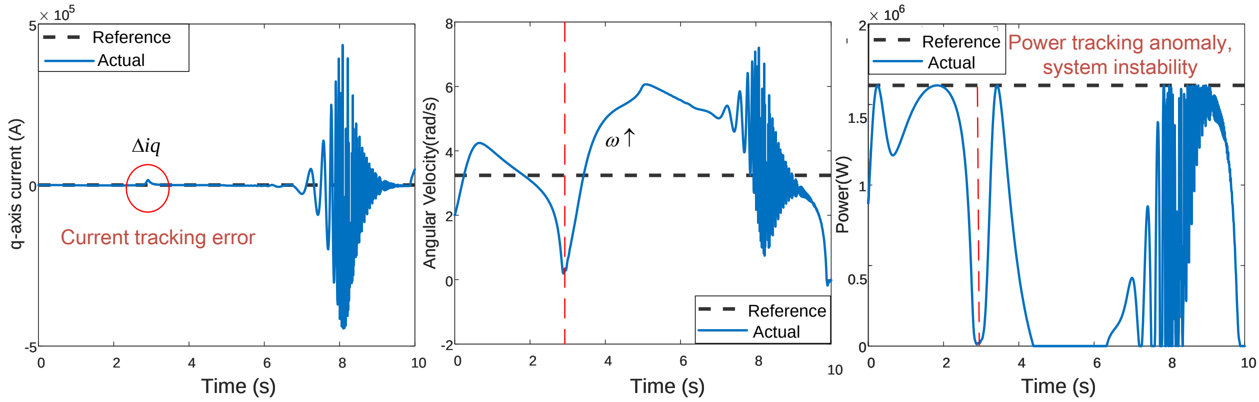

Figure 1. Impact of Inductance Mismatch on Current Tracking, Speed Response and Power Control Stability; the red dashed line indicates the moment when the inductance mismatch occurs, and the black arrow denotes the increasing trend of the rotor speed.

Regarding existing control strategies, fixed-parameter controllers frequently fail to adapt to such dynamic variations due to their reliance on predefined inductance values. Although adaptive methods can track parameter fluctuations, their practical implementation is often hampered by a large number of tuning variables and high computational complexity. Therefore, given the real-time inductance mismatch induced by long-term operation under fatigue conditions, developing a current tracking control strategy that combines parameter robustness, low computational overhead, and enhanced stability is a crucial task.

3. Design and Principles of STI-MFPCC for Robustness Against Inductance Mismatch

To address the performance degradation in tidal power generation systems—where prolonged asymmetric operation frequently induces inductance mismatch, reduces current loop robustness, and leads to unstable power output—this section proposes a self-tuning inductance-oriented model-free predictive current control (STI-MFPCC) strategy. This method leverages a simplified ultra-local model integrated with an extended state observer (ESO) to suppress non-inductive disturbances, while simultaneously achieving real-time adaptive inductance tuning via a dynamically adjusted incremental model.

3.1. Self-Tuning Inductance in Current Loop Controller

As a core component of the STI-MFPCC method, the adaptive tuning mechanism for the current loop controller identifies and compensates for dynamic inductance variations in real time. It is crucial to acknowledge that the actual magnetic saturation behavior in PMSG machines involves highly complex nonlinearities, such as cross-coupling effects and spatial harmonics. While the empirical model presented earlier captures the macroscopic degradation trend, relying on an exact analytical physical model is often computationally prohibitive and sensitive to unmodeled dynamics. To overcome this fundamental limitation, recent experimental studies have demonstrated that adopting a self-tuning incremental model can robustly track actual parameter variations without requiring a precise physical saturation model [28]. By utilizing real-time dynamic states rather than static predefined equations, this mechanism ensures robust control performance even under complex inductance mismatches. The continuous-time PMSG model is first discretized using the forward Euler method as follows:

$$\begin{cases} i_d^{k+1} = \left(1 - \frac{T_s R_s}{L_s}\right) i_d^k + \frac{T_s}{L_s} u_d^k - \frac{T_s}{L_s} E_d^k \\ i_q^{k+1} = \left(1 - \frac{T_s R_s}{L_s}\right) i_q^k + \frac{T_s}{L_s} u_q^k + \frac{T_s}{L_s} E_q^k \end{cases} \tag{6}$$

where $i_{d,q}^k$ and $u_{d,q}^k$ represent the stator current and voltage components at the k-th sampling instant, respectively; $E_{d,q}^k$ denotes the back electromotive force (EMF), and T_s is the sampling period.

Given that the sampling frequency is significantly higher than the electrical frequency ($\frac{1}{T_s} \gg 2\pi n_p \omega_m$), the back EMF is assumed to remain constant over adjacent control periods ($E_q^k \approx E_q^{k-2}$). By selecting two adjacent intervals (e.g., $[k-2, k]$ and $[k, k+2]$), the q-axis voltage equations are derived:

$$\begin{cases} \frac{u_q^{k-2} + u_q^{k-1}}{2} = R_s \frac{i_q^k + i_q^{k-2}}{2} + \frac{L_s}{T_s} \frac{i_q^k - i_q^{k-2}}{2} + E_q^{k-2} \\ \frac{u_q^k + u_q^{k+1}}{2} = R_s \frac{i_q^{k+2} + i_q^k}{2} + \frac{L_s}{T_s} \frac{i_q^{k+2} - i_q^k}{2} + E_q^k \end{cases} \tag{7}$$

To eliminate the influence of the back EMF and stator resistance (noting that $R_s \ll L_s / T_s$), the voltage and current increments are defined as:

$$\begin{cases} \Delta u_q^{k+1} = (u_q^k + u_q^{k+1}) - (u_q^{k-2} + u_q^{k-1}) \\ \Delta(\Delta i_q)^k = (i_q^{k+2} - i_q^k) - (i_q^k - i_q^{k-2}) \end{cases} \tag{8}$$

Consequently, a simplified difference model solely dependent on the stator inductance L_s is obtained:

$$\Delta u_q^{k+1} = \frac{L_s}{T_s} \Delta\left(\Delta i_q\right)^k \tag{9}$$

In the predictive controller, the voltage increment is calculated using the estimated inductance $\hat{L}_{sm}^k$ to drive the predicted current toward the reference i_{qref}^k. The relationship between the actual system response and the controller model is established by equating the voltage increments:

$$\Delta u_q^{k+1} = \frac{L_s}{T_s} (i_q^{k+2} - 2 i_q^k + i_q^{k-2}) \tag{10}$$

$$\Delta u_q^{k+1} = \frac{\hat{L}_{sm}^k}{T_s} (i_{qref}^k - 2 i_q^k + i_q^{k-2}) \tag{11}$$

By introducing an inductance correction coefficient γ^k, and considering the computational delay of the digital control system, the practical tuning laws are derived as follows:

$$\gamma^k = \frac{i_{qref}^k - 2 i_q^k + i_q^{k-2}}{i_q^{k+2} - 2 i_q^k + i_q^{k-2}} = \frac{\Delta(\Delta i_q)_{\mathrm{ref}}^k}{\Delta(\Delta i_q)^k} \tag{12}$$

$$\hat{L}_{raw}^k = \gamma^{k-2} \hat{L}_{sm}^{k-2} = \frac{i_{qref}^{k-2} - 2 i_q^{k-2} + i_q^{k-4}}{i_q^k - 2 i_q^{k-2} + i_q^{k-4}} \hat{L}_{sm}^{k-2} \tag{13}$$

The tuning process converges when $\gamma^k = 1$, indicating that the estimated inductance matches the actual value.

To mitigate potential numerical instability and high-frequency noise amplification caused by the double differential terms $\Delta(\Delta i_q)_k$, a discrete first-order low-pass filtering (LPF) strategy is integrated into the identification loop. Since inductance variations due to magnetic saturation and marine fouling occur on a significantly slower time scale than the current sampling frequency, the raw identified inductance $\hat{L}^k_{raw}$ is processed as follows:

$$\hat{L}^k_f = (1-\alpha)\hat{L}^{k-1}_f + \alpha\hat{L}^k_{raw} \tag{14}$$

where $\alpha = T_s/(\tau + T_s)$ is the smoothing factor and τ is the filtering time constant. This recursive structure effectively suppresses the jitter of the inductance correction coefficient in sensor-intensive industrial environments. Furthermore, a clamping operator is applied to constrain the filtered inductance $\hat{L}^k_f$ within a physically realistic range (e.g., $0.5\ L_n \leq \hat{L}_f \leq 1.5\ L_n$), ensuring the convergence and robustness of the self-tuning mechanism even under extreme sampling anomalies. This dual-layer protection strategy prevents the propagation of numerical oscillations into the predictive control law, thereby enhancing the overall system stability.

Finally, for interior-type PMSGs where $L_d \neq L_q$, this adaptive tuning process is extended to the d-axis to ensure comprehensive identification and compensation of dynamic inductance variations across all operating conditions.

3.2. Model-Free Predictive Current Control Based on Extended State Observer

Since the system model in PMSG is complex with excessive tunable parameters, the ultralocal model-assisted ESO enables efficient calculation of the rotor reference voltage vector, reducing reliance on precise system models. The first-order ultralocal model for a single-input single-output system is represented as follows:

$$\dot{y} = F + \alpha u_s \tag{15}$$

where u_s and y represent the control variable and output variable, respectively, α the scaling factor, and F the known and unknown components of the system. Utilizing the ultralocal model, the control law for model-free control is provided as follows:

$$u = \left(-\hat{F} + \dot{y}^* + K_p e\right)/\alpha \tag{16}$$

where $\hat{F}$ is the estimate of F, y^* the desired output, K_p the proportional gain, and e is the output tracking error. The ultralocal mathematical model of the PMSG can be represented using complex vectors as follows:

$$\frac{di_s}{dt} = F + \alpha u_s \tag{17}$$

where $F = (-R_s i_s - j\omega\psi_r)/L_s$ is assumed to be the unknown component, and $\alpha = 1/L_s$ is the gain of the input values. Based on the ultralocal model of the PMSG, a linear ESO with state variables i_s and F can be constructed, along with feedback from the current error, as follows:

$$\begin{cases} e_{rr} = \hat{i}_s - i_s \\ \dot{\hat{i}}_s = \hat{F} + \alpha u_s - \eta_1 e_{rr} \\ \dot{\hat{F}} = -\eta_2 e_{rr} \end{cases} \tag{18}$$

where $\hat{i}_s$ and $\hat{F}$ are the estimated values of i_s and F, respectively, and η_1 and η_2 are the observer's error feedback gains. The state observer can be discretized as follows:

$$\begin{cases} e_{rr}(k) = \hat{i}_s(k) - i_s(k) \\ \hat{i}_s(k+1) = \hat{i}_s(k) + T_s(\hat{F}(k) + \alpha u_s(k)) - \eta_{01} e_{rr}(k) \\ \hat{F}(k+1) = \hat{F}(k) - \eta_{02} e_{rr}(k) \end{cases} \tag{19}$$

where η_{01} and η_{02}, represent the gains of the discrete—time observer. Their values will influence the distribution of the closed-loop poles of the system (24), thereby affecting the stability of the observer. The transfer function of the ESO is given by:

$$G(z) = \frac{\hat{i}_s(z)}{i_s(z)} = \frac{\eta_{01}z - \eta_{01} + \eta_{02}T_s}{(z-1)^2 + \eta_{01}z - \eta_{01} + \eta_{02}T_s} \tag{20}$$

By setting values of the poles $z_{1,2}$ within the unit circle of the z-domain to ensure exponential convergence of the observation error, the observer gains can be determined. For the control of permanent magnet synchronous generator systems, the current inner loop must maintain a high bandwidth to meet the demands of rapid torque tracking. Considering the speed parameters of the PMSG, the speed loop bandwidth should not be less than 1 kHz. As is usually considered, the current loop is set 10 times faster, then the observer bandwidth is set to 10 kHz. For the complex PMSG system with excessive tunable parameters, the ultralocal model-assisted ESO enables efficient rotor reference voltage vector calculation and reduces precise model dependence.

3.3. Lyapunov Stability Analysis of ESO for PMSG Current Loop

To rigorously evaluate the performance of the proposed observer, the stability of the discretized ESO is analyzed. Consider the estimation error dynamics derived from the system model:

$$\mathbf{e}(k+1) = \Phi\mathbf{e}(k) + \mathbf{d}(k) \tag{21}$$

where $\mathbf{e}(k) = [e_1(k), e_2(k)]^T$ is the estimation error vector, $\mathbf{d}(k)$ represents the lumped perturbation including discretization residuals and modeling uncertainties, and the state transition matrix is defined as:

$$\Phi = \begin{bmatrix} 1-\eta_{01} & T_s \\ -\eta_{02} & 1 \end{bmatrix} \tag{22}$$

Assumption 1. *The observer gains η_{01} and η_{02} are appropriately selected such that the matrix Φ is Schur stable, meaning all its eigenvalues $\lambda_i(\Phi)$ satisfy $|\lambda_i(\Phi)| < 1$.*

Assumption 2. *The perturbation term $\mathbf{d}(k)$ is bounded, i.e., there exists a positive constant $\delta > 0$ such that $\|\mathbf{d}(k)\| \le \delta$ for all $k \ge 0$.*

Theorem 1. *Given Assumptions 1 and 2, the estimation error $\mathbf{e}(k)$ of the discrete-time ESO is Uniformly Ultimately Bounded (UUB). The error trajectory converges to a compact set $\Omega_{\mathbf{e}}$ defined by the system parameters and the perturbation bound.*

Proof. Consider a Lyapunov function candidate $V(k) = \mathbf{e}^T(k)P\mathbf{e}(k)$, where $P \in \mathbb{R}^{2\times 2}$ is a symmetric positive definite matrix. Since Φ is Schur stable, for any symmetric positive definite matrix Q, there exists a unique symmetric positive definite solution P to the discrete-time Lyapunov equation:

$$\Phi^T P \Phi - P = -Q \tag{23}$$

The forward difference of the Lyapunov function $\Delta V(k) = V(k+1) - V(k)$ is derived as:

$$\begin{aligned}\Delta V(k) &= [\Phi\mathbf{e}(k) + \mathbf{d}(k)]^T P[\Phi\mathbf{e}(k) + \mathbf{d}(k)] - \mathbf{e}^T(k)P\mathbf{e}(k) \\ &= \mathbf{e}^T(k)(\Phi^T P\Phi - P)\mathbf{e}(k) + 2\mathbf{e}^T(k)\Phi^T P\mathbf{d}(k) + \mathbf{d}^T(k)P\mathbf{d}(k)\end{aligned} \tag{24}$$

Substitution of (23) into the above expression yields:

$$\Delta V(k) = -\mathbf{e}^T(k)Q\mathbf{e}(k) + 2\mathbf{e}^T(k)\Phi^T P\mathbf{d}(k) + \mathbf{d}^T(k)P\mathbf{d}(k) \tag{25}$$

By utilizing the Rayleigh quotient property and the Cauchy-Schwarz inequality, the terms in $\Delta V(k)$ can be bounded as follows:

$$\begin{gathered}-\mathbf{e}^T(k)Q\mathbf{e}(k) \leq -\lambda_{\min}(Q)\|\mathbf{e}(k)\|^2 \\ |2\mathbf{e}^T(k)\Phi^T P\mathbf{d}(k)| \leq 2\|\Phi^T P\|\delta\|\mathbf{e}(k)\| \\ \mathbf{d}^T(k)P\mathbf{d}(k) \leq \lambda_{\max}(P)\delta^2\end{gathered} \tag{26}$$

where $\lambda_{\min}(\cdot)$ and $\lambda_{\max}(\cdot)$ denote the minimum and maximum eigenvalues, respectively. Thus, the upper bound of $\Delta V(k)$ is:

$$\Delta V(k) \leq -\lambda_{\min}(Q)\|\mathbf{e}(k)\|^2 + 2\|\Phi^T P\|\delta\|\mathbf{e}(k)\| + \lambda_{\max}(P)\delta^2 \tag{27}$$

The condition $\Delta V(k) < 0$ is satisfied if the norm of the error exceeds the following threshold:

$$\|\mathbf{e}(k)\| > \frac{\|\Phi^T P\|\delta + \sqrt{(\|\Phi^T P\|\delta)^2 + \lambda_{\min}(Q)\lambda_{\max}(P)\delta^2}}{\lambda_{\min}(Q)} \triangleq \mu \tag{28}$$

According to the Lyapunov stability theory for discrete-time systems, the estimation error $\mathbf{e}(k)$ is UUB, and the error will eventually enter the residual set $\Omega_{\mathbf{e}} = \{\mathbf{e} : \|\mathbf{e}\| \leq \mu\}$. This completes the proof. □

The radius of the convergence set μ is proportional to the perturbation bound δ. Since δ is related to the sampling period T_s, a smaller T_s (higher sampling frequency) effectively reduces the estimation error bound, enhancing the steady-state accuracy of the current loop.

3.4. Overall Control Architecture of the STI-MFPCC

The comprehensive architecture of the proposed control method is illustrated in Figure 2. Its core innovation lies in the integration of a self-tuning inductance module, which enables real-time identification and compensation for dynamic variations in the generator's inductance parameters during actual operation. This module works in synergy with the ESO and model predictive current control (MPCC) to form a robust control framework: the ESO consolidates unmodeled system dynamics and external disturbances into a generalized disturbance to facilitate effective observation and compensation; simultaneously, the MPCC leverages an updated predictive model—informed by the latest self-tuning inductance parameters—to optimize future current trajectories, thereby generating high-performance voltage commands. Ultimately, the entire system achieves precise and rapid control of generator torque and speed through coordinate transformation and the space vector pulse width modulation (SVPWM) module.

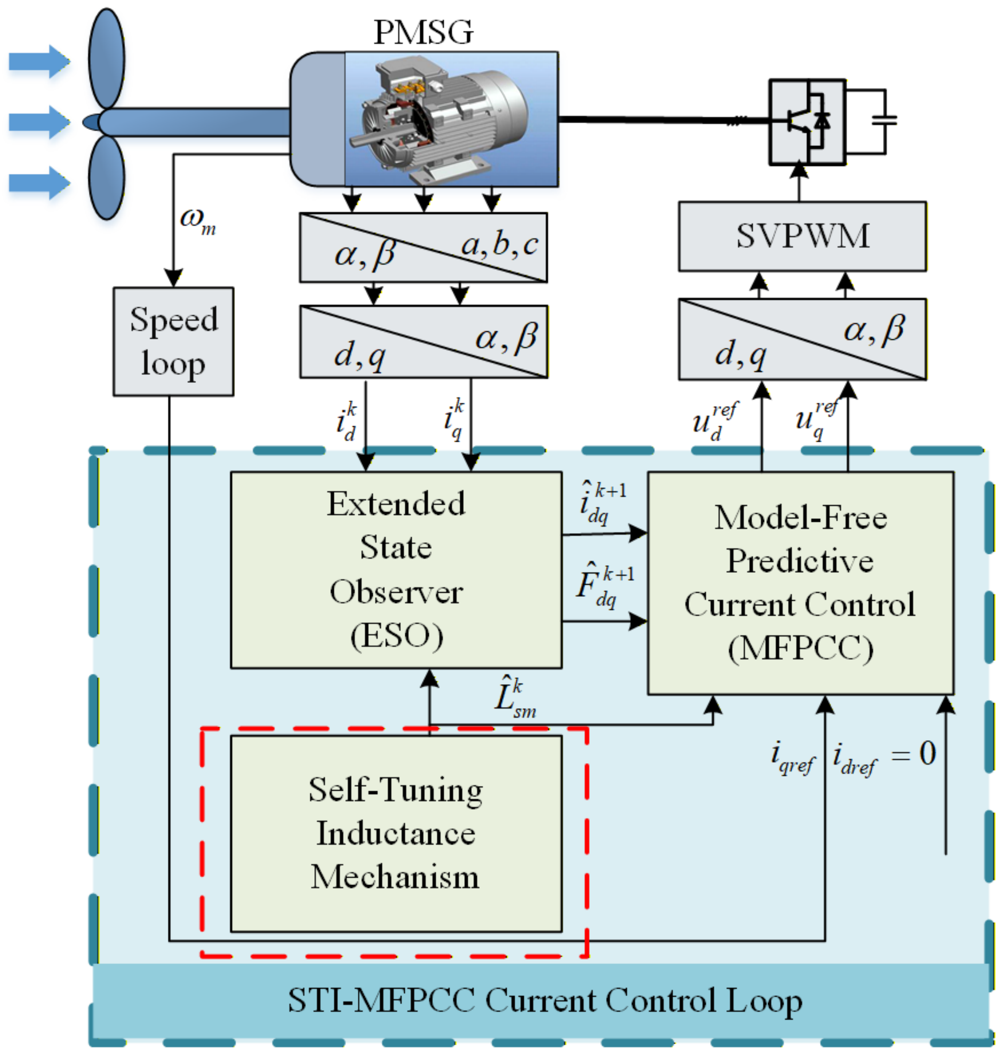

Figure 2. Control Block Diagram for the proposed STI-MFPCC on the TST generator-side, where the red dashed box highlight the core inductance tuning module.

4. Simulation Results and Analysis

To verify the effectiveness of the proposed method, real-time simulations are conducted on the RT-LAB platform (v2024.1.3.44, Opal-RT Technologies, Montreal, QC, Canada), with the corresponding results analyzed in detail.

4.1. Introduction to the TST Simulation Platform

In order to lay a solid foundation for the subsequent real-time simulation verification of the proposed method, a detailed introduction to the TST simulation platform is presented. An RT-LAB real-time model was developed based on the OPAL-RT OP5707 hardware platform (Opal-RT Technologies, Montreal, QC, Canada) and RT-LAB v2024.1.3.44 software to validate the control method. The platform effectively emulates the dynamic response of the physical system, including the PMSG and power electronics, enabling a comprehensive assessment of the control algorithm's performance, robustness, and stability under various operational scenarios without the risks and costs associated with testing on an actual turbine.

The system was modeled with a sampling period of 5×10^{-5} s, utilizing the `ode4` solver (MATLAB/Simulink R2018b, The MathWorks, Inc., Natick, MA, USA). The platform simulates a complete tidal stream turbine system, which includes the turbine, a direct-driven PMSG, and a back-to-back power converter. The PMSG is controlled by a machine-side converter that implements field-oriented control for speed and torque regulation.

To thoroughly evaluate the robustness of the proposed method under parameter mismatch conditions, simulations were conducted under three different inductance values: the rated inductance, −20% inductance deviation, and +20% inductance deviation. The parameters of the TST prototype and the PMSG are provided in Table 1. Additionally, to ensure the full reproducibility of the presented results, the key tuning parameters and coefficients for both the proposed STI-MFPCC and the comparative baseline controllers are thoroughly detailed in Table 1. Figure 3 shows the RT-LAB experimental platform.

Table 1. Key Controller Parameters and Tuning Coefficients.

Control Strategy	Parameter Description	Value
Global Settings	Sampling period (T_s)	5×10^{-5} s
	Speed loop PI proportional gain ($K_{p\omega}$)	2000
	Speed loop PI integral gain ($K_{i\omega}$)	20,000
STI-MFPCC (Proposed)	ESO bandwidth (ω_o)	10,000 rad/s
	LPF smoothing factor (α)	0.05
	Inductance clamping limits	$[0.5\ L_n, 1.5\ L_n]$
ADRC (Baseline)	ESO bandwidth (ω_{o_adrc})	4000 rad/s
	Controller bandwidth (ω_{c_adrc})	1000 rad/s
PI Current Loop	Proportional gain (K_{pc})	200
	Integral gain (K_{ic})	2000

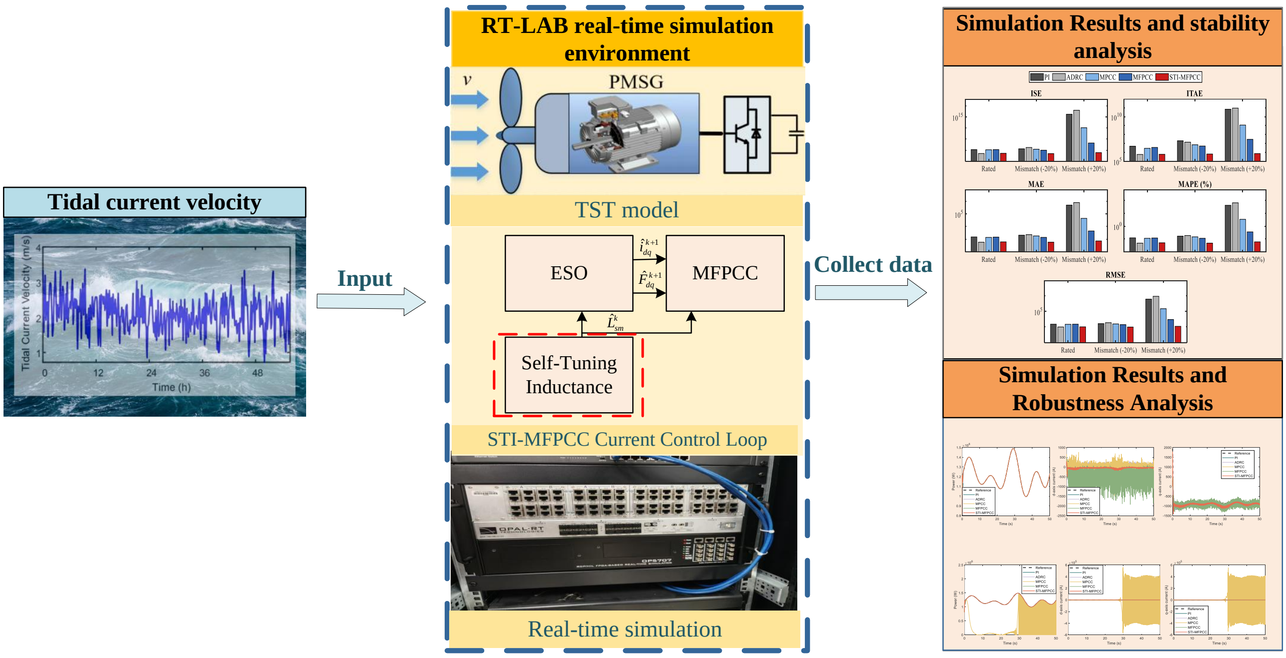

Figure 3. RT-LAB real-time simulation platform for the TST system with STI-MFPCC current control; the red dashed box indicates the self-tuning inductance module.

4.2. Stability and Efficiency Analysis of the Proposed Method Under Realistic Turbulent Disturbances

Tidal current velocity exhibits complex dynamic characteristics. The primary component is driven by predictable tidal currents resulting from the gravitational forces of celestial bodies. However, the actual velocity is also subject to significant high-frequency fluctuations caused by secondary factors such as wind waves, weather conditions, and seabed topography. These disturbances, manifesting as turbulent surges and abrupt variations, not only reduce power capture efficiency but also threaten the stability of the tidal stream turbine and PMSG system, imposing stringent requirements on the control strategy.

To accurately represent these phenomena, the total tidal stream velocity is modeled as a superposition of low-frequency steady-state components and high-frequency transient fluctuations [39]:

$$\begin{cases} v(t) = v_{\text{tide}} + v_w(t) \\ v_w(t) = \sum_i \dfrac{2\pi a_i}{T_i} \dfrac{\cosh\left(2\pi \frac{z+d}{L_i}\right)}{\sinh\left(2\pi \frac{d}{L_i}\right)} \cos 2\pi \left(\dfrac{t}{T_i} - \dfrac{y}{L_i} + \varphi_i \right) \end{cases} \tag{29}$$

where v_{tide} represents the average tidal velocity, and $v_w(t)$ denotes the wave-induced velocity derived from linear wave theory. The parameters a_i, T_i, L_i, and φ_i represent the amplitude, period, wavelength, and initial phase of the i-th wave component, respectively; y and z are the horizontal coordinate and vertical height above the seabed; and d is the water depth.

For real-time simulation verification, the inflow velocity profile is fitted based on the field measurement data from the Xihoumen Waterway (Zhoushan, Zhejiang Province, China), as shown in Figure 4, a typical high-flow-rate tidal stream energy-rich waterway in the East China Sea. The parameters of the velocity waveform are adjusted to replicate the actual tidal characteristics of the target waterway, with a sampling period of 5×10^{-5} s. Real-time simulation is implemented on the RT-LAB platform, covering a 50-s time window that fully captures the turbulent fluctuations and surge characteristics of the actual tidal current. The generated velocity waveform exhibits periodic turbulent fluctuations with an amplitude ranging from ± 0.2 m/s to ± 0.6 m/s, and a peak flow velocity of 3 m/s.

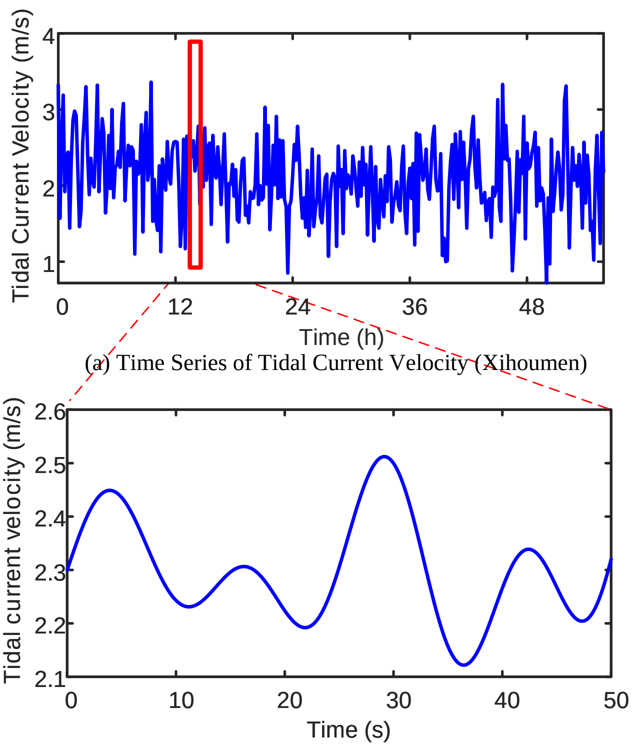

(a) Time Series of Tidal Current Velocity (Xihoumen)

(b) Magnified Tidal Current Velocity fitting segment

Figure 4. Fitted tidal current velocity profile from Xihoumen Waterway field measurements.

Under rated inductance conditions, the simulated tidal current flows into the tidal stream turbine (TST). To quantitatively evaluate the performance of the proposed control method, multiple error metrics are employed, including the integral of the squared error (ISE), integral of time-weighted absolute error (ITAE), mean absolute error (MAE), mean absolute percentage error (MAPE), and root mean squared error (RMSE), as defined in Equation (30). Dynamic response ensures that the system reaches a steady state quickly and smoothly by minimizing ITAE, avoiding excessive oscillations; Steady-state accuracy measures the error between the system output and the desired value after stabilization by minimizing MAE and MAPE, ensuring high precision over time; Overall performance considers both instantaneous and accumulated errors through ISE and RMSE, ensuring that the system provides stable and reliable control under various conditions.

$$\begin{aligned}
\mathrm{ISE} &= \int_0^{\infty} [e(t)]^2\,\mathrm{d}t \\
\mathrm{ITAE} &= \int_0^{\infty} t \cdot |e(t)|\,\mathrm{d}t \\
\mathrm{MAE} &= \frac{1}{N}\sum_{i=1}^{N}|y_i - \hat{y}_i| \\
\mathrm{MAPE} &= \frac{1}{N}\sum_{i=1}^{N}\left|\frac{y_i - \hat{y}_i}{y_i}\right| \times 100\% \\
\mathrm{RMSE} &= \sqrt{\frac{1}{N}\sum_{i=1}^{N}(y_i - \hat{y}_i)^2}
\end{aligned} \tag{30}$$

where $e(t)$ is the instantaneous error between the reference and actual value at time t, y_i is the actual system output at the i-th sampling instant, $\hat{y}_i$ is the reference value at the i-th sampling instant, N is the total number of sampling points in the evaluation period, and t is the time variable in continuous-domain evaluation.

To evaluate the proposed STI-MFPCC, RT-LAB simulations (Figures 5–8, Table 2) compare its performance against PI, ADRC, MPCC, and MFPCC schemes. Under rated inductance (Figure 5), the STI-MFPCC achieves high-fidelity current tracking. Its five error metrics (ISE, ITAE, MAE, MAPE, RMSE) closely match the optimal performance of the ADRC and significantly outperform the other benchmarks. The superiority of the STI-MFPCC is profoundly highlighted under ±20% inductance mismatches (Figures 6 and 7). While the benchmark schemes suffer severe waveform distortions—with PI and ADRC completely losing stability under a +20% mismatch—the STI-MFPCC maintains precise tracking. Quantitatively (Table 3), under a −20% mismatch, the ITAE and MAE of the STI-MFPCC are merely 3.3% and 28.2% of the PI controller's, respectively. Furthermore, under a +20% mismatch, the error metrics of the benchmarks soar by multiple orders of magnitude, whereas the STI-MFPCC maintains near-nominal precision. These results confirm the exceptional robustness of the proposed method against parameter variations, fulfilling the stringent reliability requirements of practical tidal stream applications.

4.3. Robustness Analysis of the Proposed Method

To comprehensively evaluate the industrial practicality of the proposed control strategy, rigorous robustness tests were conducted under two highly typical industrial disturbances: high-frequency measurement noise and uncompensated time delays.

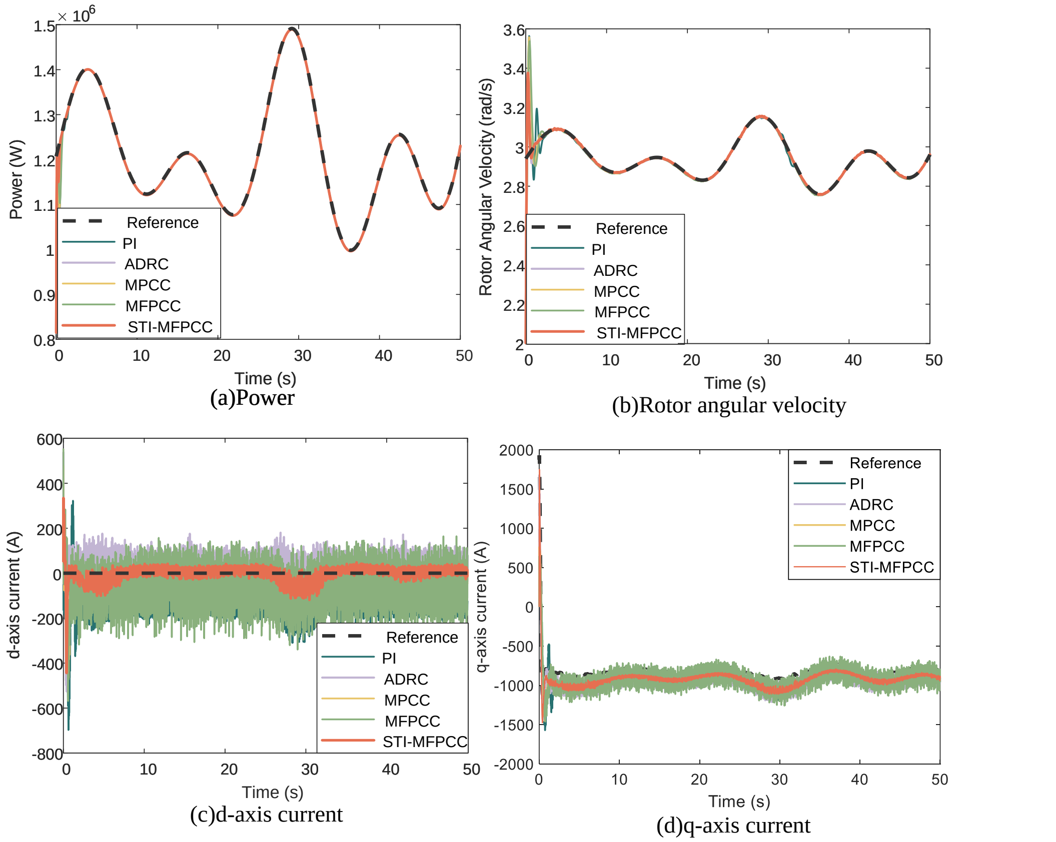

Figure 5. Comparison of various current control methods under rated inductance conditions based on a 50-s simulation.

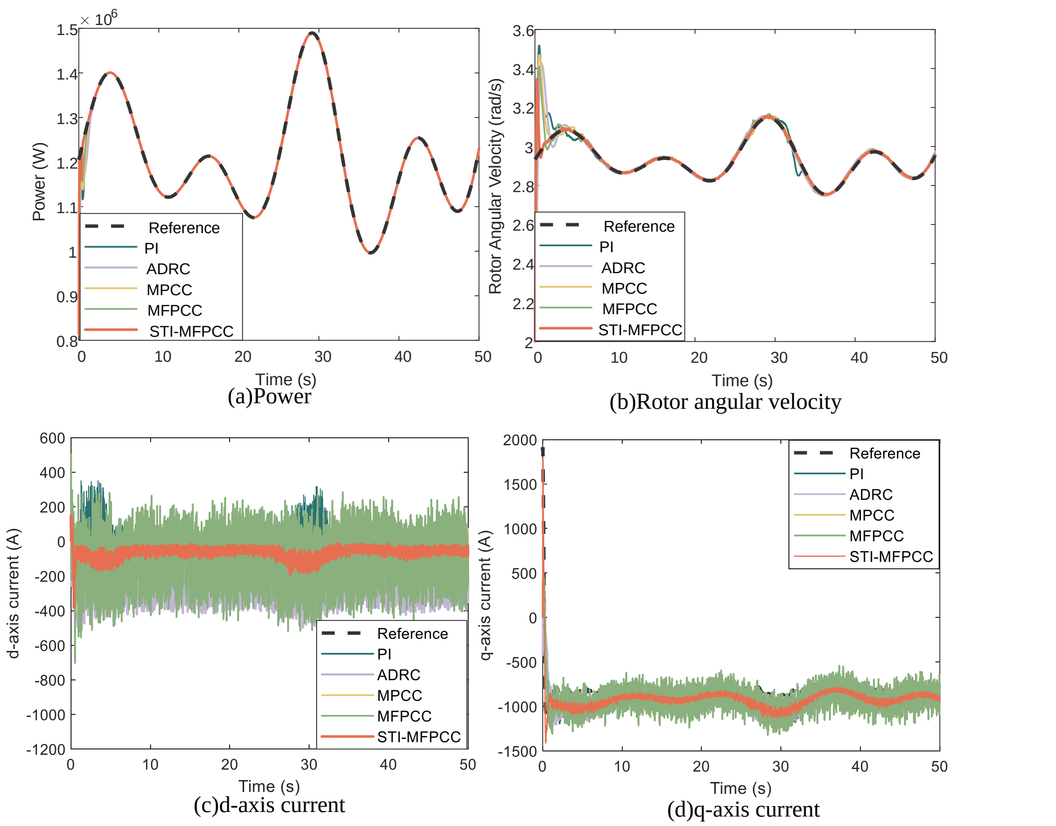

Figure 6. Comparison of various current control methods under a −20% inductance mismatch based on a 50-s simulation.

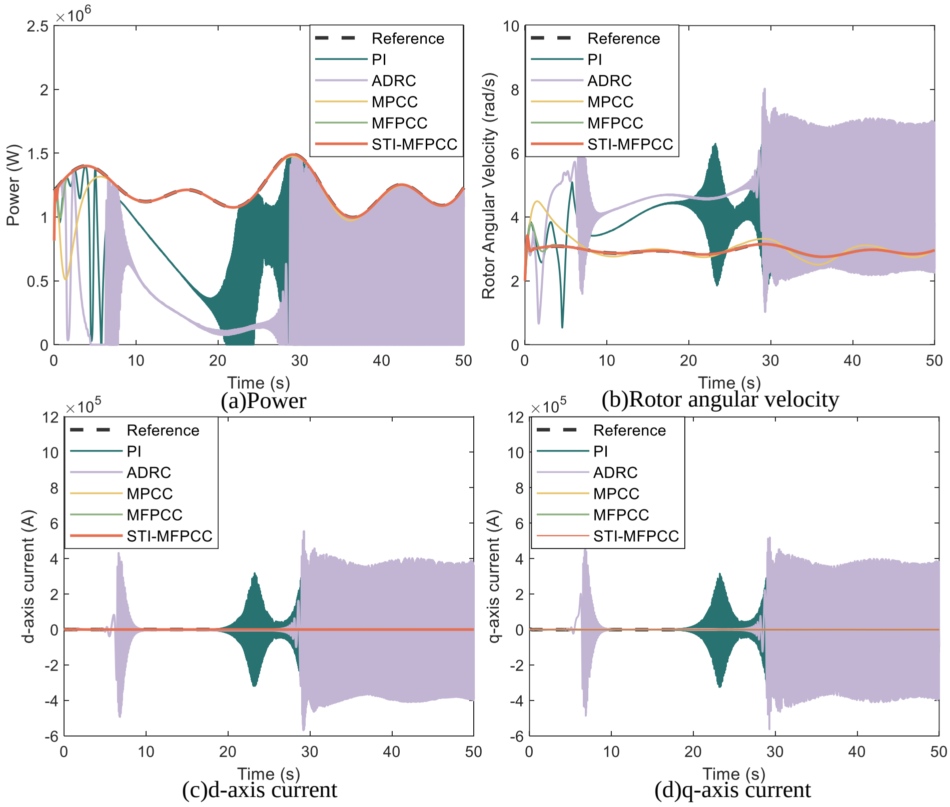

Figure 7. Comparison of various current control methods under a +20% inductance mismatch based on a 50-s simulation.

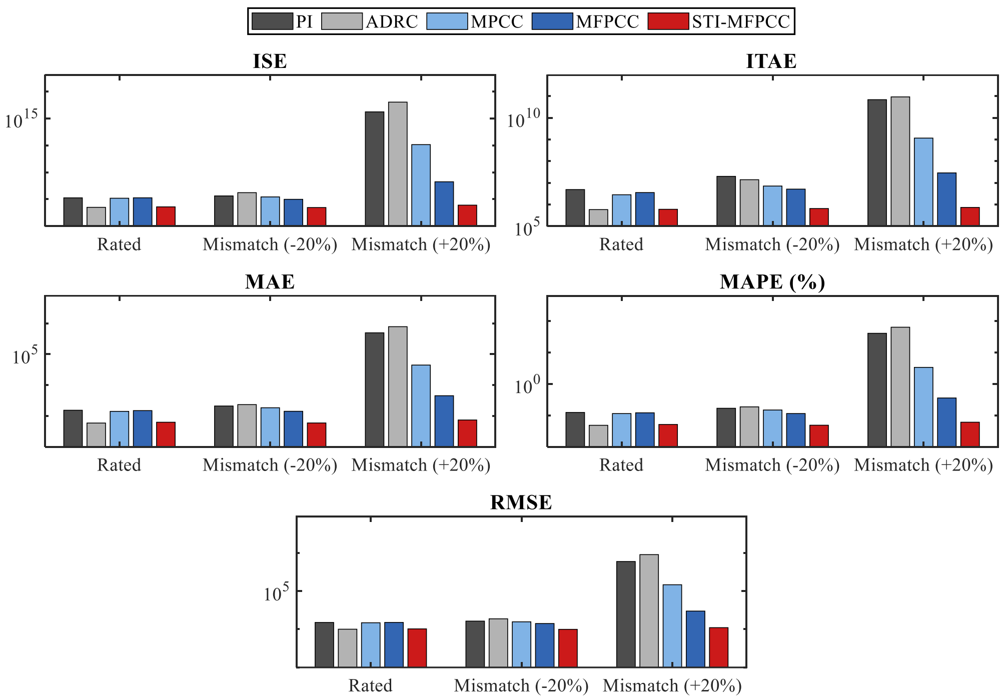

Figure 8. Statistical comparison of current performance metrics under different inductance conditions.

4.3.1. Robustness Against Measurement Noise

Current sensors in tidal turbine systems are often affected by high-frequency noise. This noise propagates through the control loop, leading to current ripples and increased mechanical stress. To test the robustness of the controllers, band-limited white noise was injected into the measured d-q axis currents ($i_{d,q}$). This setup effectively simulates typical sensor inaccuracies in industrial environments.

Table 2. Key parameters of the turbine and PMSG.

Category	Parameter	Value
Turbine	Water Density, ρ	1025 kg/m^3
	Impeller Radius, R	8.0 m
	Rated Tidal Velocity, v_{rated}	3.2 m/s
	Rated Power, P_{rated}	1.5 MW
	Optimal Tip Speed Ratio, λ_{opt}	8.1
	Max Power Coefficient, $C_{p,\max}$	0.45
PMSG	Pole Pairs, n_p	125
	Magnetic Flux, ψ_f	2.458 Wb
	Resistance, R_s	0.0081 Ω
	Stator Inductance, L_s ($L_d = L_q$)	1.20 mH
	Rated Angular Velocity, ω_{rated}	2.84 rad/s
	Inertia, J	1.313×10^5 kg · m^2

Table 3. Comparison of current performance metrics under different inductance conditions.

Condition	Method	ISE	ITAE	MAE	MAPE (%)	RMSE
Rated inductance	PI	1.13×10^{12}	4.88×10^6	1.53×10^3	0.12	1.50×10^4
	ADRC	0.50×10^{12}	0.58×10^6	0.59×10^3	0.05	1.00×10^4
	MPCC	1.09×10^{12}	2.82×10^6	1.40×10^3	0.11	1.48×10^4
	MFPCC	1.13×10^{12}	3.55×10^6	1.49×10^3	0.12	1.50×10^4
	STI-MFPCC	0.52×10^{12}	0.60×10^6	0.62×10^3	0.05	1.02×10^4
Inductance mismatch (−20%)	PI	1.33×10^{12}	19.8×10^6	2.09×10^3	0.17	1.63×10^4
	ADRC	1.76×10^{12}	13.9×10^6	2.32×10^3	0.19	1.87×10^4
	MPCC	1.22×10^{12}	7.10×10^6	1.84×10^3	0.15	1.56×10^4
	MFPCC	0.99×10^{12}	5.11×10^6	1.41×10^3	0.11	1.41×10^4
	STI-MFPCC	0.49×10^{12}	0.65×10^6	0.59×10^3	0.05	0.99×10^4
Inductance mismatch (+20%)	PI	1754×10^{12}	$68{,}183 \times 10^6$	491×10^3	40.95	592×10^3
	ADRC	4025×10^{12}	$91{,}833 \times 10^6$	775×10^3	63.96	897×10^3
	MPCC	107×10^{12}	1153×10^6	44.3×10^3	3.37	146×10^3
	MFPCC	4.45×10^{12}	28.7×10^6	4.50×10^3	0.36	29.8×10^3
	STI-MFPCC	0.60×10^{12}	0.73×10^6	0.74×10^3	0.06	11.0×10^3

The dynamic responses of active power and q-axis current under noise injection are shown in Figure 9. Root Mean Square Error (RMSE) and Mean Absolute Error (MAE) are used to quantify the tracking precision. These metrics reflect the steady-state performance and help avoid evaluation bias from random noise spikes. The quantitative results are summarized in Table 4.

As illustrated in Figure 9, baseline methods struggle to suppress the high-frequency noise. The q-axis currents for PI, ADRC, and MPCC show significant oscillations around the reference line. Specifically, their i_q RMSE values are 151.96 A, 241.96 A, and 211.08 A, respectively. These large current ripples result in heavy power oscillations. As shown in Table 4, all baseline methods exhibit a power RMSE exceeding 10,800 W, which degrades the power quality.

In contrast, the proposed STI-MFPCC achieves superior noise rejection. The q-axis current (red curve in Figure 9) follows the reference more closely and is smoother than other methods. Quantitatively, it yields the lowest i_q RMSE (118.16 A) and MAE (110.99 A). For active power, STI-MFPCC reduces the RMSE to 10,219 W and the MAE to 624.56 W.

These results demonstrate that the proposed strategy effectively filters measurement noise and ensures a stable power output.

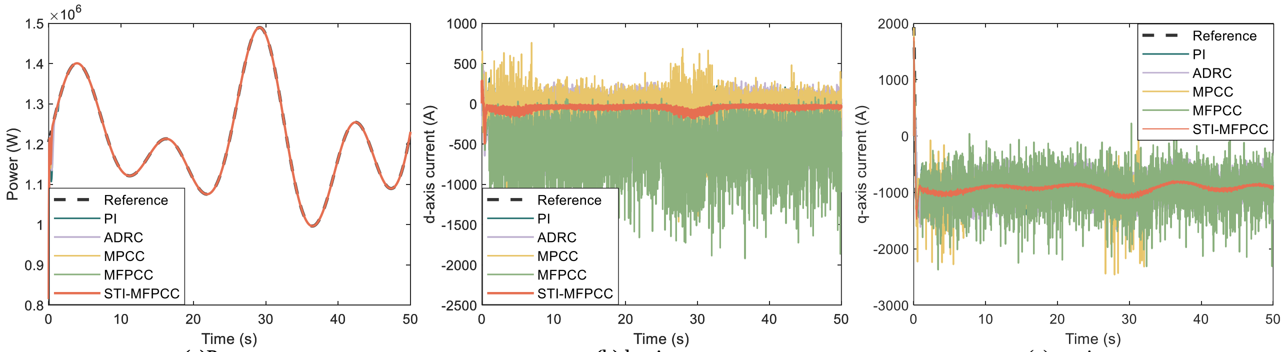

(a)Power (b)d-axis current (c)q-axis current

Figure 9. Comparison of current control methods under measurement noise conditions.

Table 4. Quantitative Performance Evaluation Under Measurement Noise (Robustness Test).

Control Strategy	q-Axis Current (i_q)		Active Power (P)	
	RMSE (A)	MAE (A)	RMSE (W)	MAE (W)
PI	151.96	120.07	13,697	1330.1
ADRC	241.96	189.86	13,484	1286.4
MPCC	211.08	142.98	10,830	699.59
MFPCC	311.79	232.23	10,767	823.92
STI-MFPCC	118.16	110.99	10,219	624.56

4.3.2. Robustness Against Time Delays

Digital control systems in tidal turbines inevitably suffer from time delays due to communication latency, signal filtering, and computational execution. These uncompensated delays cause severe phase mismatches between the predicted model and the actual physical system, severely threatening control stability. To test the robustness of the controllers, an artificial integer delay (e.g., 1.0 T_s, where T_s is the sampling period) was injected into the measured d-q axis currents ($i_{d,q}$). This setup effectively simulates severe computational or communication latencies in industrial applications.

The dynamic responses of active power and q-axis current under the injected time delay are shown in Figure 10. Similar to the noise test, Root Mean Square Error (RMSE) and Mean Absolute Error (MAE) are used to quantify the tracking degradation caused by the delay. The quantitative results are summarized in Table 5.

As illustrated in Figure 10, baseline methods exhibit high sensitivity to the time delay. The traditional MPCC is the most severely affected, as the uncompensated delay causes a severe phase mismatch in its precise mathematical model. Consequently, its tracking errors increase drastically, with the i_q RMSE and active power RMSE reaching 1.77×10^5 A and 9.93×10^5 W, respectively. Meanwhile, PI, ADRC, and MFPCC maintain basic operation but still show noticeable phase lags and significant oscillations. Specifically, the i_q RMSE values for PI, ADRC, and MFPCC increase to 138.52 A, 150.58 A, and 171.82 A, respectively. As shown in Table 5, their active power RMSEs all exceed 10,300 W (e.g., MFPCC reaches 14,195 W), which degrades the power quality.

In contrast, the proposed STI-MFPCC demonstrates superior robustness against time delays. The q-axis current (red curve in Figure 10) overcomes the phase mismatch and tracks the reference closely with minimal chattering. Quantitatively, it yields the lowest i_q RMSE (131.77 A) and MAE (124.82 A). For active power, STI-MFPCC successfully restricts the RMSE to 10,217 W and the MAE to 627.70 W. These results demonstrate that the data-driven observation mechanism effectively treats the uncompensated delays as unmodeled dynamics, thereby ensuring stable power tracking under severe communication or computational latencies.

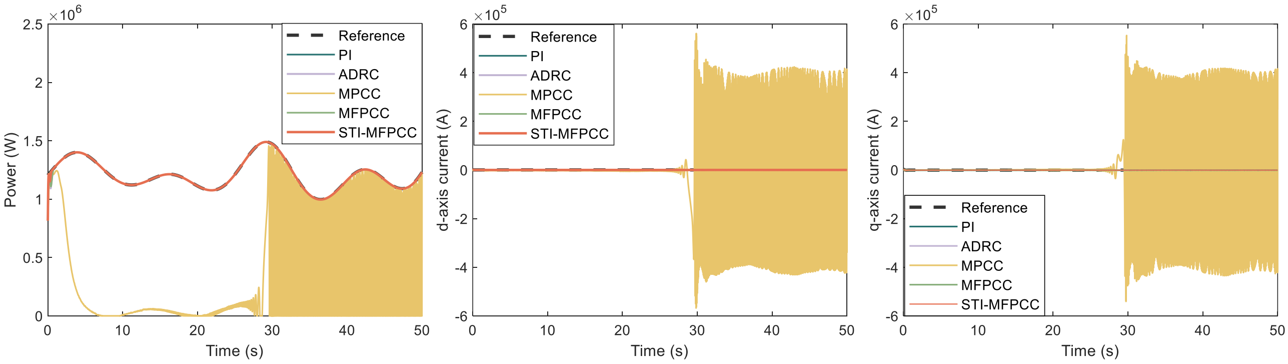

(a)Power (b)d-axis current (c)q-axis current

Figure 10. Current Control Method Comparison Under Time Delay.

Table 5. Quantitative Performance Evaluation Under Time Delay (Robustness Test).

Control Strategy	*q*-Axis Current (i_q)		Active Power (*P*)	
	RMSE (A)	MAE (A)	RMSE (W)	MAE (W)
PI	138.52	126.51	10,379	667.96
ADRC	150.58	129.68	14,054	1266.1
MPCC	1.77×10^5	1.02×10^5	9.93×10^5	8.80×10^5
MFPCC	171.82	135.11	14,195	1326.2
STI-MFPCC	131.77	124.82	10,217	627.70

5. Conclusions

To address dynamic inductance variation, measurement noise, uncompensated time delays, and unstable power output in TST systems under asymmetric loading, an STI-MFPCC method is proposed. Based on an incremental model, it achieves highly robust current control via an inductance self-tuning mechanism and a model-free framework. Its key advantages are: (1) An online self-tuning mechanism realizes real-time identification and compensation of dynamic inductance, maintaining stable current tracking even under a 20% inductance mismatch caused by magnetic saturation. (2) An ultra-local model combined with an ESO enables model-free predictive current control, significantly reducing the reliance on precise PMSG mathematical models and decreasing the computational burden. (3) Integrating a dual-layer filtering strategy with the data-driven observation capability of the ESO significantly enhances the system's immunity to external disturbances. The proposed method achieves superior noise suppression and maintains absolute stability under uncompensated digital delays, whereas conventional model-based strategies suffer from severe performance degradation or divergence. Experimental results verify its excellent stability, simple structure, and strong engineering applicability under severe parameter mismatches and typical industrial disturbances.

Future research will extend this framework to collaboratively identify multiple parameters (e.g., resistance, flux linkage) online, further validating its long-term reliability in high-power tidal turbines under complex ocean conditions.

Author Contributions: Conceptualization, M.C., T.W. and X.L.-S.; methodology, M.C. and T.W.; software, M.C.; validation, M.C., T.W. and X.W.; formal analysis, M.C., D.D. and X.L.-S.; investigation, M.C. and X.W.; resources, T.W.; data curation, M.C. and X.W.; writing—original draft preparation, M.C.; writing—review and editing, T.W., D.D. and X.L.-S.; visualization, M.C. and X.W.; supervision, T.W. and X.L.-S.; project administration, T.W.; funding acquisition, T.W. All authors have read and agreed to the published version of the manuscript.

Funding: This research was funded by the National Natural Science Foundation of China (NSFC), grant number 62573283.

Data Availability Statement: The data presented in this study are available on request from the corresponding author. The data are not publicly available due to restriction.

Conflicts of Interest: The authors declare no conflicts of interest.

Nomenclature

P_m, T_m	Mechanical power and mechanical torque of the turbine	W, N·m
ρ, v	Density of seawater and tidal stream velocity	kg/m^3, m/s
R, β	Radius of the turbine blades and pitch angle	m, rad
ω	Angular velocity of the turbine	rad/s
C_p, λ	Power coefficient and tip speed ratio	–, –
u_d, u_q	d-axis and q-axis components of stator voltage	V
i_d, i_q	d-axis and q-axis components of stator current	A
R_s	Stator resistance	Ω
L_d, L_q	d-axis and q-axis stator inductances	H
L_{d0}, L_{q0}	Rated d-axis and q-axis inductances	H
$L_s, \hat{L}_{sm}$	Nominal stator inductance and its estimated value	H
ψ_f, n_p	Permanent magnet flux linkage and number of pole pairs	Wb, –
ω_n, T_e	Rotor mechanical angular velocity and electromagnetic torque	rad/s, N·m
J, B	Combined moment of inertia and viscous friction coefficient	kg·m^2, N·m·s/rad
k_d, k_q	Saturation coefficients for d-axis and q-axis inductances	–
T_s	Sampling period	s
E_d, E_q	d-axis and q-axis back electromotive force	V
γ^k	Inductance correction coefficient at the k-th sampling instant	–
$\hat{L}^k_{raw}, \hat{L}^k_f$	Raw identified inductance and filtered inductance	H
τ, α	LPF filtering time constant and smoothing factor	s, –
$F, \hat{F}$	System lumped dynamics and its estimated value	A/s
u_s, i_s	Control variable (stator voltage) and output (stator current)	V, A
e_{rr}	Observer estimation error	A
η_{01}, η_{02}	Discrete-time observer error feedback gains	–
$\Phi, \mathbf{d}(k)$	State transition matrix and lumped perturbation vector	–, –
$V(k)$	Lyapunov function candidate	–
δ, μ	Bound of the perturbation term and radius of the convergence set	–

References

1. Chowdhury, M.S.; Rahman, K.S.; Selvanathan, V.; Nuthammachot, N.; Suklueng, M.; Mostafaeipour, A.; Habib, A.; Akhtaruzzaman, M.; Amin, N.; Techato, K. Current trends and prospects of tidal energy technology. *Environ. Dev. Sustain.* **2021**, *23*, 8179–8194. [CrossRef] [PubMed]
2. Sun, Y.; Li, Y.; Wang, R.; Ma, R. Assessing the national synergy potential of onshore and offshore renewable energy from the perspective of resources dynamic and complementarity. *Energy* **2023**, *279*, 128106. [CrossRef]
3. Chen, P.; Wu, D. A review of hybrid wave-tidal energy conversion technology. *Ocean. Eng.* **2024**, *303*, 117684. [CrossRef]
4. Liu, X.; Chen, Z.; Si, Y.; Qian, P.; Wu, H.; Cui, L.; Zhang, D. A review of tidal current energy resource assessment in China. *Renew. Sustain. Energy Rev.* **2021**, *145*, 111012. [CrossRef]
5. Zhang, D.; Yang, K.; Zhang, H.; Yang, K.; Zeng, S.; Si, K.; Zhang, Y. Challenges in tidal energy commercialization and technological advancements for sustainable solutions. *iScience* **2025**, *28*, 112348. [CrossRef]
6. Bebars, A.D.; Eladl, A.A.; Abdulsalam, G.M.; Badran, E.A. Internal electrical fault detection techniques in DFIG-based wind turbines: A review. *Prot. Control. Mod. Power Syst.* **2022**, *7*, 1–22. [CrossRef]

7. Zhu, Z.; Wang, X.; Yan, B.; Li, L.; Wu, Q. A dynamic decoupling control method for PMSM of brake-by-wire system based on parameters estimation. *IEEE/ASME Trans. Mechatron.* **2021**, *27*, 3762–3772. [CrossRef]
8. Zhang, Y.; Jiang, T. Robust predictive rotor current control of a doubly fed induction generator under an unbalanced and distorted grid. *IEEE Trans. Energy Convers.* **2021**, *37*, 433–442. [CrossRef]
9. Zhang, Y.; Jiang, T. Robust predictive stator current control based on prediction error compensation for a doubly fed induction generator under nonideal grids. *IEEE Trans. Ind. Electron.* **2021**, *69*, 4398–4408. [CrossRef]
10. Venkaiah, P.; Sarkar, B.K. Hydraulically actuated horizontal axis wind turbine pitch control by model free adaptive controller. *Renew. Energy* **2020**, *147*, 55–68. [CrossRef]
11. Civelek, Z.; Lüy, M.; Çam, E.; Mamur, H. A new fuzzy logic proportional controller approach applied to individual pitch angle for wind turbine load mitigation. *Renew. Energy* **2017**, *111*, 708–717. [CrossRef]
12. Surinkaew, T.; Ngamroo, I. Robust power oscillation damper design for DFIG-based wind turbine based on specified structure mixed H_2/H_∞ control. *Renew. Energy* **2014**, *66*, 15–24. [CrossRef]
13. Asl, H.J.; Yoon, J. Power capture optimization of variable-speed wind turbines using an output feedback controller. *Renew. Energy* **2016**, *86*, 517–525. [CrossRef]
14. Karabacak, M.; Fernández-Ramírez, L.M.; Kamal, T.; Kamal, S. A new hill climbing maximum power tracking control for wind turbines with inertial effect compensation. *IEEE Trans. Ind. Electron.* **2019**, *66*, 8545–8556. [CrossRef]
15. Liu, Y.; Lyu, M.; Huang, S.; Liao, W.; Liang, G.; Feng, C.; Wu, X.; Huang, S. Direct torque control schemes for dual three-phase PMSM considering unbalanced DC-link voltages. *IEEE Trans. Energy Convers.* **2023**, *39*, 229–242. [CrossRef]
16. Vijayalakshmi, P.; Sivasankar, S.; Karthikeyan, G. Simulation of wind turbine system using field oriented control and Levenberg-Marquardt Back Propagation (LMBP) neural network model. *Biomed. Signal Process. Control.* **2024**, *92*, 105961. [CrossRef]
17. Ouchen, S.; Benbouzid, M.; Blaabjerg, F.; Betka, A.; Steinhart, H. Direct power control of shunt active power filter using space vector modulation based on supertwisting sliding mode control. *IEEE J. Emerg. Sel. Top. Power Electron.* **2020**, *9*, 3243–3253. [CrossRef]
18. Liu, X.; Deng, Y.; Liu, J.; Cao, H.; Xu, C.; Liu, Y. Fixed-time integral terminal sliding mode control with an adaptive RBF neural network for PMSM speed regulation. *Control. Eng. Pract.* **2025**, *156*, 106236. [CrossRef]
19. Moumani, Y.; Laafou, A.J.; Ait Madi, A. Backstepping and ADRC control performances applied to wind turbine. In *Proceedings of the 2022 IEEE 3rd International Conference on Electronics, Control, Optimization and Computer Science (ICECOCS)*; IEEE: Piscataway, NJ, USA, 2022; pp. 1–5.
20. Wang, C.; Fan, Z.; Meng, J.; Sun, Y.; Zhou, Z.; Cui, J. Active disturbance rejection control strategy for permanent magnet synchronous wind power system. In *Proceedings of the 2023 8th Asia Conference on Power and Electrical Engineering (ACPEE)*; IEEE: Piscataway, NJ, USA, 2023; pp. 811–815.
21. Lin, P.; Zhang, S.; Wu, Z.; Li, J.; Sun, X.M. A linear-nonlinear switching active disturbance rejection voltage controller of PMSG. *IEEE Trans. Transp. Electrif.* **2022**, *8*, 3367–3378. [CrossRef]
22. Hollweg, G.V.; de Oliveira Evald, P.J.D.; Tambara, R.V.; Gründling, H.A. A robust adaptive super-twisting sliding mode controller applied on grid-tied power converter with an LCL filter. *Control. Eng. Pract.* **2022**, *122*, 105104. [CrossRef]
23. Salem, A.A.; Aldin, N.A.N.; Azmy, A.M.; Abdellatif, W.S.E. Implementation and validation of an adaptive fuzzy logic controller for MPPT of PMSG-based wind turbines. *IEEE Access* **2021**, *9*, 165690–165707. [CrossRef]
24. Benbouhenni, H.; Bizon, N.; Mosaad, M.I.; Colak, I.; Djilali, A.B.; Gasmi, H. Enhancement of the power quality of DFIG-based dual-rotor wind turbine systems using fractional order fuzzy controller. *Expert Syst. Appl.* **2024**, *238*, 121695. [CrossRef]
25. Song, D.; Liu, J.; Yang, Y.; Yang, J.; Su, M.; Wang, Y.; Gui, N.; Yang, X.; Huang, L.; Joo, Y.H. Maximum wind energy extraction of large-scale wind turbines using nonlinear model predictive control via Yin-Yang grey wolf optimization algorithm. *Energy* **2021**, *221*, 119866. [CrossRef]
26. Agoro, S.; Husain, I. Model-free predictive current and disturbance rejection control of dual three-phase PMSM drives using optimal virtual vector modulation. *IEEE J. Emerg. Sel. Top. Power Electron.* **2022**, *11*, 1432–1443. [CrossRef]
27. Zhang, Y.; Jiang, T.; Jiao, J. Model-free predictive current control of DFIG based on an extended state observer under unbalanced and distorted grid. *IEEE Trans. Power Electron.* **2020**, *35*, 8130–8139. [CrossRef]
28. Wang, H.; Gan, C.; Zhang, C.; Ren, H.; Qu, R. Parameter Robust Predictive Current Control for PMSM Drives Based on Self-Tuning Incremental Model and Voltage Constraint Compensation. *IEEE Trans. Power Electron.* **2025**, *40*, 11268–11282. [CrossRef]
29. Wang, Z.; Chai, J.; Xiang, X.; Sun, X.; Lu, H. A novel online parameter identification algorithm designed for deadbeat current control of the permanent-magnet synchronous motor. *IEEE Trans. Ind. Appl.* **2022**, *58*, 2029–2041. [CrossRef]
30. Lei, J.; Fang, S.; Huang, D.; Wang, Y. Enhanced deadbeat predictive current control for PMSM drives using iterative sliding mode observer. *IEEE Trans. Power Electron.* **2023**, *38*, 13866–13876. [CrossRef]
31. Gaamouche, R.; Redouane, A.; El Harraki, I. Optimal feedback control of nonlinear variable-speed Tidal Stream Turbines using a two-mass model. *J. Mar. Sci. Appl.* **2020**, *19*, 83–95. [CrossRef]

32. Zouheyr, D.; Lotfi, B.; Abdelmadjid, B. Improved hardware implementation of a TSR-based MPPT algorithm for a low cost connected wind turbine emulator under unbalanced wind speeds. *Energy* **2021**, *232*, 121039. [CrossRef]
33. Shu, H.; Wang, G.; Chen, J.; Ma, H.; He, T. Coordinated control of wind-storage combined with primary frequency regulation and variable coefficient based on wind speed and SOC. *J. Energy Storage* **2024**, *87*, 111356. [CrossRef]
34. Majout, B.; El Alami, H.; Salime, H.; Zine Laabidine, N.; El Mourabit, Y.; Motahhir, S.; Bouderbala, M.; Karim, M.; Bossoufi, B. A review on popular control applications in wind energy conversion system based on permanent magnet generator PMSG. *Energies* **2022**, *15*, 6238. [CrossRef]
35. Kariman, H.; Hoseinzadeh, S.; Khiadani, M.; Nazarieh, M. 3D-CFD analysing of tidal Hunter turbine to enhance the power coefficient by changing the stroke angle of blades and incorporation of winglets. *Ocean. Eng.* **2023**, *287*, 115713. [CrossRef]
36. Xie, T.; Wang, T.; He, Q.; Diallo, D.; Claramunt, C. A review of current issues of marine current turbine blade fault detection. *Ocean. Eng.* **2020**, *218*, 108194. [CrossRef]
37. Xu, Y.; Wang, T.; Diallo, D.; Amirat, Y. A confidence-guided DS fault diagnosis method for tidal stream turbines blade. *Ocean. Eng.* **2024**, *311*, 118807. [CrossRef]
38. Lu, Y.; Huang, K.; Wang, B.; Lai, C.; Feng, G. Data-driven modeling and compensation strategy of PMSM considering core loss and saturation. *IEEE J. Emerg. Sel. Top. Power Electron.* **2024**, *12*, 1894–1905. [CrossRef]
39. Junejo, A.K.; Xu, W.; Mu, C.; Ismail, M.M.; Liu, Y. Adaptive speed control of PMSM drive system based on a new sliding-mode reaching law. *IEEE Trans. Power Electron.* **2020**, *35*, 12110–12121. [CrossRef]